Mammatus Clouds as a Response to Cloud-Base Radiative Heating

TIMOTHY J. GARRETT, CLINTON T. SCHMIDT, AND STINA KIHLGREN

Department of Atmospheric Sciences, University of Utah, Salt Lake City, Utah

CÉLINE CORNET

Laboratoire d'Optique Atmospherique, Université des Sciences et Technologies de Lille, Villeneuve d'Ascq, France

(Manuscript received 25 March 2010, in final form 25 August 2010)

ABSTRACT

Mammatus clouds are the pouchlike lobes seen hanging from mid- to high-level clouds. They can look quite dramatic, but they are also interesting because they provide clues to what controls anvil cirrus dynamic evolution. Thus far, the most commonly accepted explanation for observed subsidence of mammatus lobes is that they are driven by evaporative cooling of precipitation, accelerated by mixing with dry subcloud air. Here, an alternative explanation is proposed: radiative temperature contrasts between cloud base and the lower troposphere destabilize cloudy air to create a rapidly deepening mixed layer, which creates positively buoyant intrusions of dry air into the cloud interior; mammatus lobes are just the descending branch of the resulting circulations. In this regard, mammatus cloud fields might be considered an upside-down analog to the radiatively driven formation of ''cloud holes'' seen at the tops of stratocumulus layers.

1. Introduction

The outflow from deep convection into the free troposphere plays a crucial component in the atmospheric redistribution of energy and water vapor (Manabe and Strickler 1964; Soden 1998). Condensation amplifies interactions of electromagnetic radiation with matter, and because cirrus anvils tend to be high and thermally opaque (Hartmann and Larson 2002), they provide a mechanism for efficient radiation of terrestrial energy to space.

However, remarkably few theoretical and observational studies have explored how the deposition and emission of radiative energy in cirrus clouds influences their dynamic evolution (Starr and Cox 1985; Lilly 1988; Fu 1996; Gu and Liou 2000; Dobbie and Jonas 2001; Garrett et al. 2005; Dinh et al. 2010). In this paper, we investigate its potential role in a particularly visually appealing perspective of this problem: mammatus clouds, the smooth, laminar cloud formations that are sometimes seen hanging from the base of cirrus anvils (Schultz et al. 2006) and even volcanic clouds (Durant et al. 2009). Near sunset, their side illumination can make for astonishingly dramatic and beautiful skies.

The most commonly cited explanation for mammatus is that they are the visible portion of negatively buoyant thermals that are created by the descent of large hydrometeors near cloud base. Especially if the subcloud air is dry, precipitation cools the air while it sublimates, propelling the lobes further downward. It was this mechanism that was shown to be responsible in the first numerical simulations to reproduce mammatus-like structures (Schultz et al. 2006; Kanak and Straka 2006; Kanak et al. 2008).

What we focus on here is another possible explanation for mammatus formation, namely that they are a consequence of radiatively driven destabilization of anvil cloud base. Also, we investigate whether dry lower-troposphere layers tend to be associated with mammatus formation not because of any sublimation mechanism, but rather because they correspond to higher atmospheric infrared transparency. We propose that increased transparency amplifies the magnitude of thermal contrasts between cloud base and upwelling atmospheric radiation, and that this determines the power of a localized heat engine supporting mammatus cloud motions.

The approach we take here is idealized, in that it is designed less to reproduce a particular event than to

Corresponding author address: Tim Garrett, 135 S. 1460 E, Room 819, Salt Lake City, UT 84112.
E-mail: tim.garrett@utah.edu

DOI: 10.1175/2010JAS3513.1

elucidate the controlling mechanisms responsible for mammatus development. To this end, we consider what idealized conditions would be required to reproduce mammatus clouds in high, cold cirrus anvils. To constrain the driving physics to a possible role for cloud radiative heating, the numerical modeling simulations do not allow for gravitational settling of cloud particles or the production of precipitation. Also, simulations of mammatus are examined for two contrasting cases of lower-troposphere humidity. Ultimately, mammatus is a visual classification, so model output is passed through a three-dimensional radiative transfer solver to produce a representation of how the naked eye might perceive idealized model representations of the cloud dynamics.

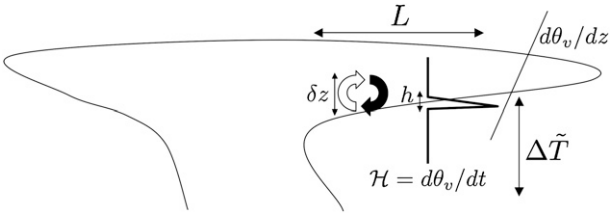

FIG. 1. Schematic of radiatively induced stabilization of anvil cloud base. Circulations are created at anvil cloud base because a radiative temperature contrast $\Delta\tilde{T}$ between anvil base and the lower troposphere leads to localized heating at a rate $\mathcal{H} = d\theta_v/dt$ within a layer of depth h, and this drives a deepening mixed layer of depth δz. To create instability, the cloud width L must be large and the heating gradient $\mathcal{H}/h$ must be sufficiently concentrated to overcome the initial anvil cloud stability ($d\theta_v/dt > 0$).

2. Theoretical arguments

Emanuel (1981) attributed mammatus development to what was termed cloud-base detrainment instability (CBDI). Instability at cloud base is amplified by evaporative cooling of hydrometeors caused by lateral entrainment of dry air into downward propagating thermals. By applying similarity theory arguments to the mass, momentum, heat, and water budgets for cloudy thermals, Emanuel provided approximate analytic solutions for mammatus lobe depth and vertical speed that were approximately consistent with available observations.

Arguably, however, what the CBDI theory lacks is a detailed mechanism for the origins of buoyant instability at cloud base. Anvil cirrus are stratiform and float within a vertically stratified atmosphere (Garrett et al. 2005), so there should be natural inhibition to any interfacial mixing across the base, although an ad hoc form of cloud-base instability proposed by Kanak et al. (2008) is to suppose that instability originates from prescribed cloud-base variability in hydrometeor gravitational loading.

An alternative mechanism for cloud-base instability is illustrated in Fig. 1. An anvil cloud base has a lower radiative emission temperature than the below-cloud lower troposphere. Cloudy air has a high infrared absorption cross-sectional density so this radiative temperature contrast is associated with radiative flux convergence at rate ΔF_{net} within the cloud. Convergence is concentrated within a cloud layer of depth h extending upward from cloud base. The increase in energy density within this layer causes the (virtual) potential temperature θ_v to warm at rate

$$\mathcal{H} = \frac{d\theta_v}{dt} = -\frac{1}{\rho c_p(1+\gamma)}\frac{dF_{\text{net}}}{dz} \simeq -\frac{1}{\rho c_p}\frac{\Delta F_{\text{net}}}{h}, \quad (1)$$

where c_p is the specific heat capacity, ρ the air density, and $\gamma = L/c_p(dq_v^{\text{sat}}/dT)$, where is L the latent heat of vaporization and q_v^{sat} the saturation vapor mixing ratio (Arakawa and Schubert 1974); also,

$$\theta_v = \theta(1 + 0.61q_v - q_i), \quad (2)$$

where θ is the potential temperature, q_v the water vapor mixing ratio, and q_i the ice water mixing ratio. For typical cirrus cloud temperatures, $\gamma \ll 1$ and the negative feedback associated with latent heating is sufficiently small to be neglected (Heymsfield and Miloshevich 1991). If the cloud is sufficiently thick to act as an approximate thermal blackbody, then radiative heating rates are approximately zero both above and below the layer of depth h. Radiative heating of the cloudy air may be sufficiently rapid to initiate a convecting mixed layer that deepens for as long as heating is applied.

The blackbody condition, and the average value of $\mathcal{H}$ within the layer, can easily be estimated. Consider that, in general, the infrared flux emissivity of a cloud is given by (e.g., Stephens et al. 1990)

$$\varepsilon_c \simeq 1 - \exp(-\tau_{\text{abs}}/\overline{\mu}), \quad (3)$$

where τ_{abs} is the absorption optical depth and $\overline{\mu}$ is a quadrature cosine suitable for estimating the integrated contribution of thermal isotropic radiation to upward or downward radiative fluxes. Normally, $\overline{\mu} \simeq 0.6$ (Herman 1980). The absorption optical depth is related to the cloud mixing ratio q_i and cloud particle effective radius r_e through $\tau_{\text{abs}} = k(r_e)q_i\rho\Delta z$, where k is the mass-specific absorption cross-sectional density. Thus, a cloud is nearly opaque to thermal radiation provided that $\tau_{\text{abs}} \gtrsim 2$ at thermal wavelengths. This is equivalent to an extinction optical depth at visible wavelengths greater than about 4, assuming particles are larger than about 20-μm radius (Yang et al. 2000).

If the cloud is thermally opaque, the *e*-folding penetration depth for the deposition of thermal radiation into cirrus is

$$h = \frac{\overline{\mu}}{d\tau_{\rm abs}/d\Delta z} = \frac{\overline{\mu}}{k(r_e)q_i\rho}. \quad (4)$$

A reasonable value for $k(r_e)$ is $\sim$0.045 m^2 g^{-1} assuming 20-μm r_e ice particles (Knollenberg et al. 1993; Garrett et al. 2005); for a moderately thick anvil, values of q_i might be 1 g kg^{-1} (or $\sim$0.4 g m^{-3}). Similar values were seen within the interior of a medium-sized Florida cirrus anvil by Garrett et al. (2005) approximately 1 h after it began detraining from deep convection. Values reaching 2 g kg^{-1} may be seen in larger anvil cirrus (Heymsfield 1986; Garrett 2008). Assuming $q_i = 1$ g kg^{-1} and $r_e = 20$ μm, thermal radiation deposition is concentrated within a depth $h \sim 30$ m at cloud base.

The rate at which radiative energy is deposited over this depth is related to the difference between the effective emission (or brightness) temperature of the anvil cirrus $\tilde{T}_c$ and the lower troposphere below the cloud $\tilde{T}_a$. In general, thermal emission from a blackbody takes the form $F = \sigma\tilde{T}^4$. The fourth power is a consequence of emission being proportional to the radiation pressure, where the radiation pressure is one-third the photon energy density (Zemanksy and Dittman 1997). Assuming $\Delta\tilde{T} = \tilde{T}_a - \tilde{T}_c \ll \tilde{T}_c$, an approximate expression for the rate of energy deposition at cloud base is

$$\Delta F_{\rm net} \simeq -4\sigma\tilde{T}_c^3\Delta\tilde{T}, \quad (5)$$

where σ is the Stefan–Boltzmann constant, an expression equivalent to the speed of light c times the local gradient in photon pressure. Gradients in photon pressure drive energetic flows into the colder cloud, increasing the energy density within the cloudy absorption layer of depth h. From Eq. (1), this causes a rise in the potential temperature of the molecules in cloudy air at a rate given by

$$\mathcal{H} = \frac{d\theta_v}{dt} = -4\sigma\tilde{T}_c^3\Delta\tilde{T}\frac{k(r_e)q_i}{\overline{\mu}c_p}. \quad (6)$$

If the potential temperature increases sufficiently quickly (see discussion below), a buoyant instability develops. Instability production is greatest if values of q_i are high and there are large thermal contrasts $\Delta\tilde{T}$ between the cloud and the lower atmosphere.

We now look at how lower-troposphere water vapor concentrations play an important role in determining the value of $\Delta\tilde{T}$. Provided the value of gh/c_p is small, where g is the gravitational acceleration and g/c_p is the approximate vertical lapse rate of atmospheric temperature at cold temperatures, the value $\tilde{T}_c$ is nearly equivalent to the kinetic temperature of gas molecules at cloud base T_c. On the other hand, $\tilde{T}_a$, includes contributions from both the surface and atmospheric thermal emission. In a simplified representation with a single-layer greenhouse atmosphere, with atmospheric kinetic temperature T_a and surface temperature T_s,

$$\tilde{T}_a^4 = T_s^4 + \varepsilon_a(T_a^4 - T_s^4), \quad (7)$$

where ε_a is the infrared emissivity of the atmospheric layer. Looking now at Eqs. (5) and (7), this implies that a radiatively transparent lower troposphere, with low values of ε_a, has warmer $\tilde{T}_a$. This effectively increases the size of the "heat engine" $\Delta\tilde{T}$ driving radiative flux deposition at cloud base.

Water vapor is the primary atmospheric constituent that absorbs infrared radiation. Water vapor absorption lines are saturated at frequencies close to their normal modes. In this case, the atmospheric absorptivity of such "strong lines" goes approximately as the square root of the water path (Liou 2002). It follows that the approximate dependence on relative humidity (RH) is $\varepsilon_a \propto \sqrt{\rm RH}$. High heating rates at cloud base should then be expected to be modestly dependent on there being low values of lower-troposphere relative humidity. Effectively, when the air between cloud base and the surface is dry, the lower atmosphere and surface warm the cloud more efficiently, accelerating radiatively induced destabilization of cloud base.

The radiative destabilization mechanism described above is not complementary to Emanuel's cloud-base detrainment instability mechanism. The CBDI mechanism is associated with a negatively buoyant perturbation that causes detrainment of negatively buoyant thermals that are propelled downward from cloud base and amplified by hydrometeor evaporative cooling. On the other hand, the radiative destabilization we describe here is associated with a source of *positive* buoyancy at cloud base that, as pointed out by Heymsfield and Miloshevich (1991), is *diminished* by cloud evaporative cooling [Eq. (1)], although only to a negligible degree if the cloud is cold. Radiative instability should be expected to propel air upward rather than downward. Fields of such radiatively driven mammatus cloud fields can be long lived because the lower troposphere acts as a large heat capacitor that sustains $\Delta\tilde{T}$ that drives instability.

It is important here to recognize, however, that radiative heating of cloud base only leads to local instability under special circumstances: instead, the cloud might simply loft as a whole (Ackerman et al. 1988). To better understand the conditions that favor destabilization near cloud base, consider as an initial condition a horizontally finite cloud

with some characteristic half-width L that is everywhere neutrally buoyant with respect to its stratified, clear-air surroundings, and whose base is heated radiatively at rate $\mathcal{H} = d\theta_v/dt$ over some characteristic h (Fig. 1).

In the absence of any dynamic response to the heating, the radiatively heated layer of cloud warms, and initially flat isentropic surfaces are bent downward with speed $\mathcal{H}/(d\theta_v/dz)$. The dynamic response that would maintain approximately flat isentropic surfaces is for air to rise at the same rate, with velocity $w_{\text{strat}} = \mathcal{H}/(d\theta_v/dz) = \mathcal{H}g/(\theta_v N^2)$. Conservation of mass requires circulations, so the rising motion requires outflow above the heating and inflow below. Assuming constant air density, divergence is zero (i.e., $\nabla \cdot \mathbf{u} = 0$), and dimensional arguments imply that the outflow speed is approximately $u_{\text{strat}} \sim w_{\text{strat}}L/h = \mathcal{H}gL/(\theta_v N^2 h)$. The response of cloudy air to radiative heating is to slowly loft and spread (e.g., Dinh et al. 2010).

However, if w_{strat} is high, and isentropes are bent down very rapidly, then the horizontal spreading rate u_{strat} required to keep isentropes flat might be "too fast." Isentropes are bent downward so quickly that a potential instability develops. A convecting mixed layer develops near cloud base with the average property of $d\theta_v/dz \sim 0$. Since the cloud's clear-air surroundings are stratified with $d\theta_v/dz > 0$, the mixed layer is therefore in a state of gravitational disequilibrium. Equilibrium is restored through either viscous dissipation of turbulence or the conversion of gravitational potential energy to kinetic energy. In a cloud of finite L, a density current may spread the mixed layer outward with speed $u_{\text{mix}} \sim Nh$, assuming the mixed layer initially has a depth h.

To evaluate what exactly represents a value of u_{strat} that is too fast in the convecting case, the above suggests a comparison of u_{strat} to u_{mix} to give a dimensionless "spreading number," introduced previously by Garrett et al. (2005):

$$\mathcal{S} = \frac{u_{\text{strat}}}{u_{\text{mix}}} \sim \frac{\mathcal{H}gL}{\theta_v N^3 h^2}. \tag{8}$$

If $u_{\text{strat}} > u_{\text{mix}}$ or $\mathcal{S} > 1$, heating will not drive laminar ascent and outflow of air while isentropic surfaces stay approximately flat. Rather, a turbulent mixed layer will develop near cloud base that spreads as a density current. This condition is favored when the cloud is wide, cold, and optically dense.

Seen another way, radiative energy is deposited at rate ΔF_{net} [Eq. (5)] within a layer of depth h [Eq. (4)] and horizontal cross section L^2 (Fig. 1). Assuming that there is a mixed layer at cloud base that has, on average, constant θ_v over a depth $\delta z \geq h$, the deposited radiative energy quickly becomes evenly dispersed through the entire mixed layer depth, diluting its effect by a factor of $\delta z/h$. Radiative heating of this mixed layer creates a growing contrast with the environment of the mixed layer. It increases the energy density that is available to drive dynamic flows in the layer Δg (or equivalently, the pressure difference) at rate $d\Delta g/dt = -R\Delta F_{\text{net}}/(c_p \delta z)$, where R is the gas constant; the remaining fraction $(c_p - R)/c_p$ of radiative enthalpy deposition goes into increasing the internal energy density of the air. The second law requires dynamic flows that act to restore equilibrium by reducing Δg in the mixed layer volume.

The available Δg in the mixed layer can be expressed as the product of the density of air in the mixed layer ρ and the gravitational potential per unit mass available to drive turbulent motions ΔG. Here, $\rho = m/V \sim m/(\delta z L^2)$, where m is the mass of air in the mixed layer, and $\Delta G \sim N^2 \delta z^2$, where N quantifies the stratification of surrounding air at the same level. Assuming that there is no entrainment of air across the mixed layer boundaries (i.e., m is fixed), evolution of the potential energy density $\Delta g = \rho \Delta G$ of the cloud can be expressed in terms of two partial differentials: the evolution of the potential per unit mass at constant density, and the evolution of the air density at constant potential:

$$\begin{aligned} \frac{d\ln\Delta g}{dt} &= \left.\frac{\partial \ln \Delta G}{\partial t}\right|_{\rho} + \left.\frac{\partial \ln \rho}{\partial t}\right|_{\Delta G} \\ &= 2\left.\frac{\partial \ln \delta z}{\partial t}\right|_{L} - 2\left.\frac{\partial \ln L}{\partial t}\right|_{\delta z}. \end{aligned} \tag{9}$$

At constant L, radiative heating increases the potential energy density of the cloud by bending isentropic surfaces downward. If a mixed layer has formed, the mixed layer deepens by gradually eroding the stably stratified air in the cloud interior. But it does so not with speed w_{strat}, which would apply to gradual lofting of the radiatively heated layer of depth h as discussed above, but rather with speed $w_{\text{strat}}h/\delta z$: radiative energy deposited in the layer of depth h is now evenly dispersed through a mixed layer depth δz. Thus, the mixed layer deepens at rate

$$\left.\frac{\partial(\delta z)}{\partial t}\right|_{L} \sim w_{\text{strat}}\frac{h}{\delta z} = \frac{\mathcal{H}gh}{\theta_v N^2 \delta z}. \tag{10}$$

Conversely, if the mixed layer is held at a constant potential level δz, the potential energy density of the mixed layer adjusts toward equilibrium through expansion of the mixed layer into its lower potential environment. The mixed layer spreads laterally along constant potential surfaces (or isentropes) with speed $dL/dt \sim N\delta z$.

Thus $\mathcal{S}$ can be seen as a measure of a magnitude of the disequilibrium in Eq. (9) that is created by an imbalance between the rate of increase in the gravitation potential

energy density at rate $\alpha_{\delta z} \sim 2\partial \ln \delta z/\partial t|_L = 2\mathcal{H}gh/(\theta_v N^2 \delta z^2)$ and the loss of potential energy density due to mixed layer expansion at rate $\alpha_L \sim 2\partial \ln L/\partial t|_{\delta z} = 2N\delta z/L$. Evaluating $\mathcal{S}$ for a cloud that is initially at rest, in which case $\delta z \sim h$, we get

$$\mathcal{S} = \frac{\alpha_{\delta z}}{\alpha_L} = \frac{\partial \ln \delta z/\partial t|_L}{\partial \ln L/\partial t|_{\delta z}} \sim \frac{\mathcal{H}gL}{\theta_v N^3 h^2}. \tag{11}$$

If $\mathcal{S} \leq 1$, then a mixed layer never develops: isentropes stay flat with the equilibrium condition of $d\ln\Delta g/dt = 0$. In this case, $\delta z = h$ and from Eq. (9), $\partial \ln L/\partial t|_{\delta z} = \partial \ln h/\partial t|_L$, leading to the previously derived solution for laminar spreading $dL/dt = u_{\text{strat}} = w_{\text{strat}}L/h$. Cloud base is warmed as it gradually lofts upward and pushes cloud above it outward.

If, however, $\mathcal{S} > 1$, then the radiatively driven disequilibrium grows sufficiently rapidly that a mixed layer develops. Equilibrium is restored through expansion of the mixed layer along isentropic surfaces into its clear-sky surroundings. This spreading allows the potential energy of the mixed layer to decrease at rate α_L. However, because $\mathcal{S} > 1$, then from Eq. (9) $\partial \ln L/\partial t|_{\delta z} = \partial \ln h/\partial t|_L$ or $\alpha_L < \alpha_{\delta z}$. The radiatively heated mixed layer deepens at a faster rate than it spreads.

The conditions that favor values of $\mathcal{S} > 1$ are some combination of the cloud being wide, concentrated heating at cloud base, and low static stability. We propose that mixed layer convection near cloud base takes on the appearance of mammatus lobes only when values of $\mathcal{S}$ are very high, such that $\alpha_{\delta z} \gg \alpha_L$ and radiative energy deposition goes almost entirely toward deepening a mixed layer. When $\mathcal{S} \gg 1$, Eq. (10) approximates a total differential (i.e., L evolves slowly or the cloud layer is effectively infinitely wide), and assuming no entrainment and that $\Delta\tilde{T}$ is fixed, the approximate solution for the mixed layer depth δz as a function of time Δt is

$$\delta z \sim \left(\frac{g\mathcal{H}h}{\theta_v N^2}\Delta t\right)^{1/2}. \tag{12}$$

From Eq. (1), $\rho c_p \mathcal{H}h$ is just the net deposition rate per unit area of radiative energy $|\Delta F_{\text{net}}|$, which itself is determined only by $\Delta\tilde{T}$ [Eq. (5)]. Thus, Eq. (12) can be expressed as

$$\delta z \sim \left(\frac{4\sigma \tilde{T}_c^3 \Delta\tilde{T}}{\rho c_p d\theta_v/dz}\Delta t\right)^{1/2}. \tag{13}$$

Radiative temperature contrasts $\Delta\tilde{T}$ drive mixed layer deepening by working against the atmospheric static stability $d\theta_v/dz$. But there are diminishing returns, since mixed layer deepening also dilutes the density of radiative energy that is deposited in the cloud. Deepening only goes as $\Delta t^{1/2}$. A more general form of this time dependence is given by Turner [1979, his Eq. (9.2.9)].

3. Numerical setup

In what follows, we use the framework of a numerical cloud model to test the above hypothesized mechanism for production of mammatus cloud. Simulations focus on an idealized tropical cirrus anvil that is wide and optically dense in which the fall speed of hydrometeors is set to zero.

Numerical simulations are performed using the University of Utah Large Eddy Simulation Model (UU LESM) (Zulauf 2001). The UU LESM is specifically designed to examine small-scale, short-period atmospheric flows, particularly those involving cloud-scale processes such as convection, entrainment, and turbulence. It includes a sophisticated interactive radiative transfer solver (Fu et al. 1995). The dynamic framework is based on the 3D nonhydrostatic primitive equations. Rather than using an anelastic set of governing equations, the quasi-compressible approximation is used in which the speed of sound is artificially reduced to 50 m s^{-1}. Damping sound waves improves computational efficiency while maintaining accuracy (Droegemeier and Wilhelmson 1987). The microphysics employs a "saturation adjustment scheme" in which cloud particles are completely sublimated in subsaturated air while in cloudy air the relative humidity is fixed at 100%, here with respect to ice (Krueger et al. 1995a). Hydrometeors contribute to the gravitational loading of an air parcel, but cloud mode particles do not settle. Precipitation mode particles can be produced in the model through diffusion and collection; however, as will be described, this option is turned off. Previously, the code has been used to study aspects of a wide range of cloud systems, including convection, anvil cirrus, and arctic stratus (e.g., Garrett et al. 2006, 2009). Here, simulations employ a periodic model domain that is 30 km × 30 km in horizontal extent, ranging from the surface to 17-km altitude in the vertical. A sponge layer is implemented above 14 km to minimize wave reflection off the top. The surface temperature is fixed at 28°C and a standard tropical profile is used.

The standard profile in this experiment is modified in two ways. First, a cloud is placed in the domain that is 2.5 km deep, with 20-km diameter, and with cloud base at 8.8-km altitude. Microphysically, the cloud is defined by a uniform ice water mixing ratio of 1 g kg^{-1} and a fixed r_e of 20 μm (e.g., Garrett et al. 2005). Cloud-base temperature is set to 242 K. Cloud tops are chosen to be at 210 K, a value chosen to be consistent with the average anvil top temperature expected in the tropics under the fixed anvil temperature hypothesis (Hartmann and Larson 2002):

cloud top was found to sublimate rapidly if it was shifted to higher levels. The virtual potential temperature profile of this idealized anvil cirrus layer, accounting for both water vapor and hydrometeor loading, is identical to that in the environmental sounding such that initially the cloud is neutrally buoyant. Initial stability values near cloud base are $d\theta_v/dz = 4.0$ K km^{-1} or $N = 0.011$ s^{-1}. The production of a precipitation mode from cloud mode particles is turned off in the model and the cloudy air is initially saturated with respect to ice. In addition, only thermal radiation is considered, Coriolis forces are absent, and the initial wind field is everywhere zero. The purpose of this setup design is that, if model radiation is turned off in the simulations, the cloud does not evolve. Radiation is the sole source for initiating any form of cloud evolution.

To highlight model cloud sensitivity to radiative destabilization, a second modification is made to the atmospheric profile. To limit sensitivity to sublimation effects in developing mammatus lobes, subcloud sublimation is artificially inhibited by specifying an atmospheric humidity of 90% with respect to ice in a 1-km-deep layer just below the initial cloud base at 8.8 km (Fig. 2). Model sensitivity to lower-troposphere humidity below 7.8-km altitude is simulated through two scenarios: a ''dry'' scenario with a relative humidity of 10% with respect to water and a ''moist'' scenario with a relative humidity of 90%. These two scenarios correspond to an initial $\tilde{T}_a$ of 279 and 269 K for the dry and moist scenario, respectively. Since cloud-base temperature is 242 K, this means that $\Delta\tilde{T}$ determining the size of the radiative heat engine destabilizing cloud base [Eq. (5)] is 37 K in the dry scenario and 27 K in the moist scenario, a difference of 37%.

The spatial resolution of the UU LESM was chosen to be sufficiently small as to resolve the skin depth h for the interactions of thermal radiation with air at cloud base, with 1 g kg^{-1} for q_i, $r_e = 20$ μm, and a radiative absorption depth of $h = 30$ m [Eq. (4)]. In the horizontal domain, resolution was set to 30 m, and in the vertical, a stretched grid was employed with a minimum spacing of 30 m in the center of the cloud domain. For dynamic calculations, the model time steps were set to 1.0 and 60 s for radiative transfer calculations. All model simulations extended for 1 h. The results described here are robust insofar as model resolution and domain size is concerned. Increasing model vertical resolution from 100 to 30 m, while decreasing the horizontal domain size from 40 to 30 km, made negligible differences to the study conclusions.

4. Numerical results

Figure 3 shows surface plots of q_i for the initial cloud disk and for its appearance after 1 h of model simulation time. Figure 4 shows a plan view of the cloud evolution.

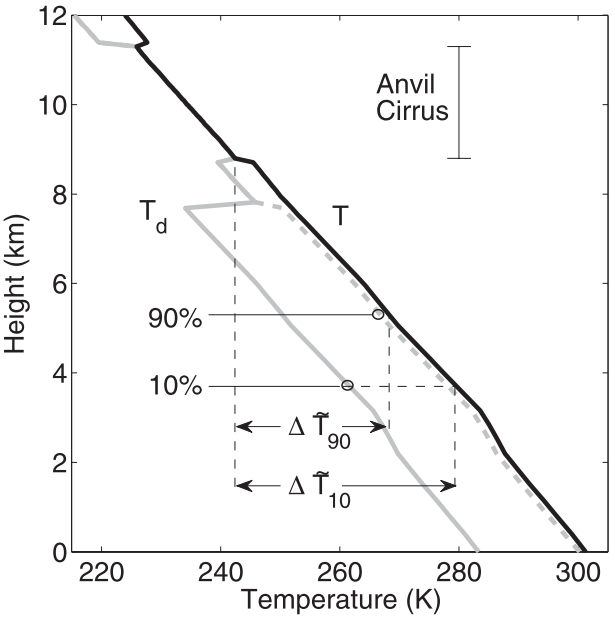

FIG. 2. Dewpoint temperature and temperature profiles for a dry (10% RH) and a moist (90% RH) lower-troposphere scenario. The temperature associated with each circle corresponds to $\Delta\tilde{T}_a$ at cloud base. Here $\Delta\tilde{T}$ represents the brightness temperature contrast determining the size of the radiative heat engine destabilizing cloud base.

In both the moist and dry lower-troposphere humidity scenarios, radiative interactions with cloud mass drive a variety of physical phenomena at cloud base. However, the most apparent response to radiative heating is not stratified ascent, as proposed by Ackerman et al. (1988), but rather horizontal spreading (see also Garrett et al. 2005, 2006; Dinh et al. 2010) and the development of lobes at cloud base. The depth and size of the cloudy lobes is largest in the case with low values of lower-troposphere relative humidity.

The formation mechanism and physical characteristics of these lobes is now studied in closer detail. The plan view of the cloud in Fig. 4 shows the extent of the cloud at initialization and at 1-h age. At 1 h the cloud has spread from 10-km radius to 12.3-km radius. For further study, we focus on a 3000-m-wide annulus of cloud base centered at a radial distance of 5500 m from cloud center.

Within this region, and as shown in Fig. 5, initial heating rates near cloud base are high, approximately 350 K day^{-1} in the dry scenario and 240 K day^{-1} in the moist scenario, a difference approximately consistent with the 37% differential magnitude of the heat engine $\Delta\tilde{T}$ [Eq. (6)]. Because the cloud is sufficiently thick to be a blackbody, the thermal radiation field within the cloudy interior is isotropic, meaning zero net flux deposition and heating. The consequence is very sharp heating gradients at cloud base. The heating gradients are sharper and the

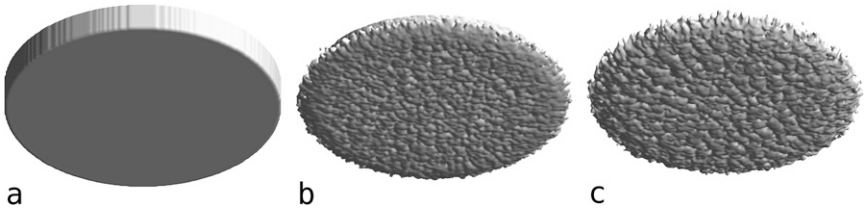

FIG. 3. A 3D view of the simulated cases showing a 0.1 g kg^{-1} cloud surface artificially illuminated to highlight cloud shape. (a) The cloud initial condition. Surface plots for the state after 1-h model simulation for the (b) 90% and (c) 10% lower-troposphere humidity scenarios.

heating rates higher than those calculated for tropical anvils by Ackerman et al. (1988), but this is because we assumed the anvil to be composed of somewhat smaller ice crystals with a higher condensate mixing ratio, guided by remote sensing measurements (Cooper and Garrett 2010) and airborne measurements using bulk microphysical probes capable of sampling small ice crystals (Garrett et al. 2005).

Taking the dry and moist lower-troposphere humidity cases presented here, values of $\mathcal{S}$ [Eq. (8)] are 970 and 670, respectively. As expected for large values of $\mathcal{S}$, the sharp heating gradients act to create a spreading and deepening mixed layer. While Fig. 5 shows that the heated layer is initially very narrow, of depth ~100 m, after 1-h simulation time it evolves to become a 724-m-deep mixed layer in the dry scenario and a 622-m-deep mixed layer in the moist scenario. The corresponding mixed layer depths δz that are predicted by Eq. (12) for this time step are 590 and 490 m, so in this aspect there is rough consistency between theory and the simulations. Above and below the mixed layer, levels of turbulent kinetic energy are near zero. Averaged over the mixed layer, values are 0.034 W kg^{-1} in the dry case and 0.024 W kg^{-1} in the moist scenario.

The mixed layer may define a broad volume where average vertical gradients in potential temperature are zero. However, the mixed layer is not in equilibrium when it is examined on smaller scales. Rather, the mixed layer is turbulent, and so it is continually in a process of dynamic adjustment around an equilibrium "well mixed" condition. In fact, in the 10% lower-troposphere humidity scenario at 1-h simulation time, 98% of mixed layer columns in the annular region contained at least one resolved layer that was characterized by a superadiabatic lapse rate, as it would be defined on a thermodynamic chart by a negative vertical gradient in the equivalent potential temperature $\theta_e \simeq \theta[1 + Lq_v/(c_pT)]$. No superadiabatic layers with $d\theta_e/dz < 0$ K km^{-1} were present below 8880 m or above 9800 m, and the peak incidence was at an altitude of 9110 m, just above the base of the mixed layer. A probability distribution function for $d\theta_e/dz$ between 8500- and 9500-m altitude, spanning cloud base at 8800-m altitude, is shown in Fig. 6. There are regions of extremely high stability just below the mixed layer, but superadiabatic regions as well. In atmospheric soundings, mammatus clouds are often associated with the presence of superadiabatic layers near cloud base (Schultz et al. 2006). Our simulations shown here indicate that superadiabatic layers should be expected when sampling a column of cloud that is being driven out of equilibrium by rapid radiative heating near the column bottom.

Figure 6 shows a conserved-variable mixing diagram in total water content (vapor plus ice) q_{tot} and $\theta_e \simeq \theta[1 + Lq_v/(c_pT)]$ (Paluch 1979) for the layer between 8500 and 9500 m in the annular region at 1-h simulation time. For the most part, the cloudy mixed layer has a very narrow range of values of (θ_e, q_{tot}) that lie along the initial cloud profile. As the mixed layer is heated, and isentropic surfaces are bent downward, the mixed layer becomes increasingly characterized by values of θ_e and q_{tot} that are representative of the initial conditions deeper within the

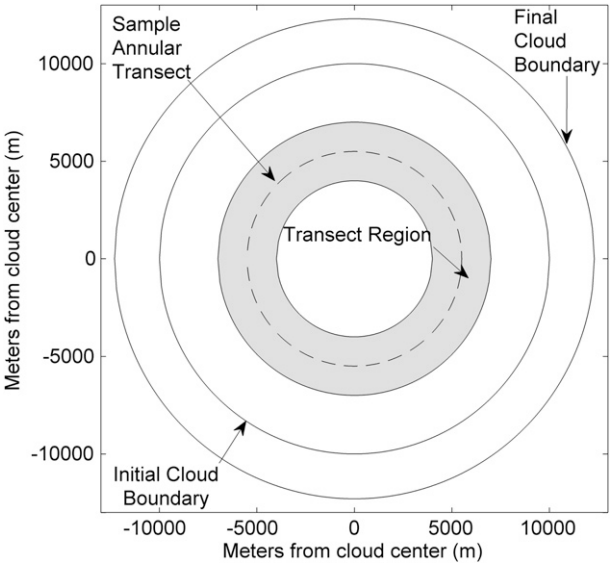

FIG. 4. Plan view of cloud base illustrating the initial cloud boundary, the cloud boundary at 1-h simulation time for the dry lower-troposphere humidity case, and the annular region centered at 5500-m radius that is used for detailed analysis of model simulations.

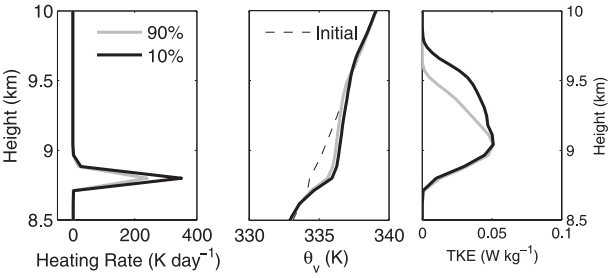

FIG. 5. Profiles of averages over the annular domain shown in Fig. 4 for (left) $\mathcal{H} = d\theta_v/dt$ at 0 s simulation time, and (middle) θ_v and (right) TKE at 1-h simulation time. The initial θ_v profile is indicated by a dashed line.

cloud. Air below cloud base has low values of θ_e and q_{tot}. A smaller portion of the mixed layer comes from parcels of air that are initially below cloud and are heated, which increases their value of θ_e. These parcels then mix almost linearly with cloudy mixed layer air. Thus, the mixed layer evolution is determined primarily by the flow of radiative energy into the cloud, and to a lesser degree by entrainment of dry air from below cloud base.

A closer look at the development of a mixed layer with some interfacial mixing at cloud base is shown in Fig. 7, which shows the model state at 1-h simulation time for the dry lower-atmosphere scenario. Isentropic surfaces within the cloud interior have become bent downward toward the original cloud base, creating an extremely highly stratified layer right below cloud base and a much more weakly stratified layer about 700 m above cloud base. The weakly stratified layer has vigorous updrafts and downdrafts and has spread outward along isentropic surfaces, as described by the two partial differentials in Eq. (11). However, a few downdrafts in the turbulent layer penetrate a few tens of meters below the initial cloud base into the stable layer below, perhaps encouraging entrainment of below-cloud dry air as penetrative convection does work on the clear-air stable layer that lies below the cloudy mixed layer (see Turner 1979). Note that a mixed layer and penetrative convection are also seen at the anvil cloud top near 11.3-km altitude where there is concentrated cloud radiative cooling rather than heating.

Figure 8 shows q_i, q_{tot}, and wind speed vectors within the annular region near cloud base (Fig. 4). In both the dry and moist case, lobed structures are evident at cloud base, associated with downdrafts in the high q_i lobes and updrafts on either side. However, in the dry lower-troposphere humidity case associated with larger below-cloud radiative temperature contrasts, the lobes are larger and deeper. As mentioned previously, both the dry and moist cases correspond to values of $\mathcal{S}$ that are sufficiently high to sustain mammatus development within a deepening, spreading mixed layer. However, mixed layer growth is slowest and has smaller, shallower lobes in the moist lower-troposphere humidity scenario with a smaller value of $\mathcal{S}$.

Within the annulus, maximum updrafts are 2.6 and 2.3 m s^{-1} in the dry and moist scenarios, respectively. Respective maximum downdrafts are -1.8 and 1.9 m s^{-1}. These values are in the range of those seen in mammatus lobes by radar (Winstead et al. 2001; Kollias et al. 2005) and aircraft (Stith 1995), although observed updraft velocities are weaker. This difference can be explained by velocities in measurements applying only to the cloudy mammatus lobes themselves whereas model results apply more to the cloud-free regions that surround the descending mammatus lobes.

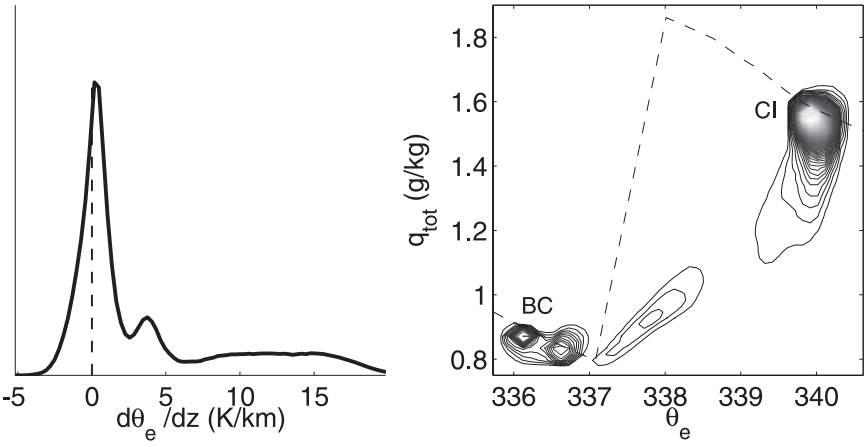

FIG. 6. PDFs for thermodynamic variables over a depth between 8500 and 9500 m within the annular domain shown in Fig. 4, and at 1-h model run time. (left) PDF for the vertical gradients in θ_e representing atmospheric stability. (right) Contoured PDF for a conserved variable diagram in θ_e and q_{tot}. The dashed line represents the initial profile, BC the initial conditions below cloud base, and Cl the initial conditions within the cloud.

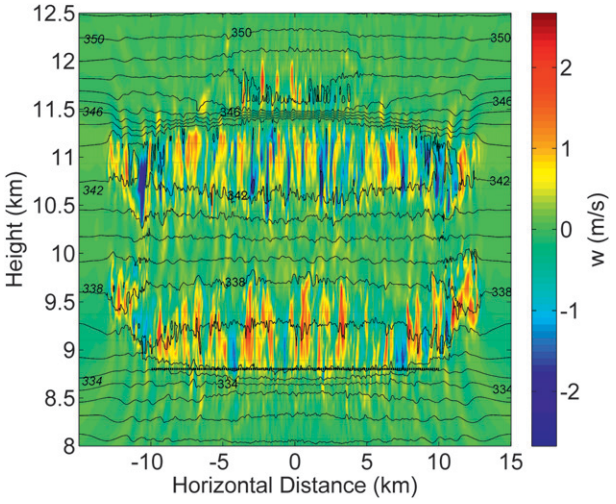

FIG. 7. Cross section of model θ_v (contours) and w (colors) at 1-h simulation time. Light dotted lines are the initial θ_v contours and the thick dotted line is the initial extent and height of cloud base.

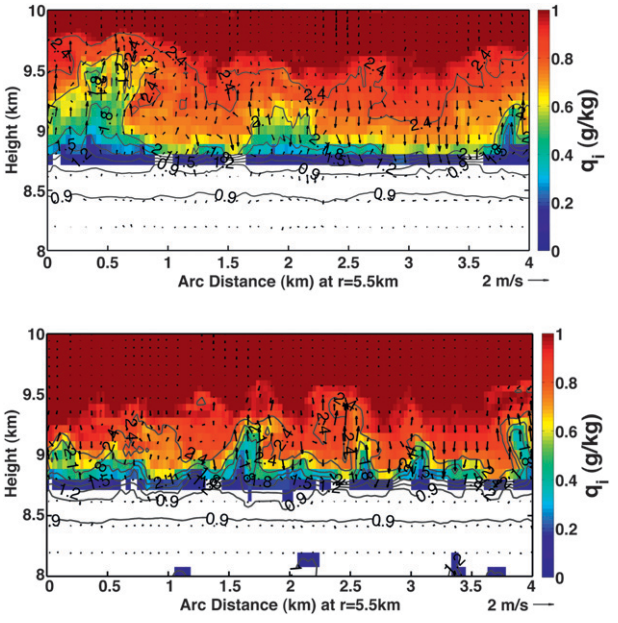

FIG. 8. Cross section along an arc at 5500-m radius of q_i (colors), wind velocity (vectors), and $q_{\rm tot}$ (contours) after 1-h simulation for a (top) dry (10% lower-troposphere RH) and (bottom) moist (90% lower-troposphere RH) scenario.

This distinction between the dry and moist cases is also evident in the difference between the wavenumber spectra in variance of w and q_i shown in Fig. 9. Calculated power spectra are the averages of 50 individual spectra from adjacent 30-m-wide circular transects within the annulus shown in Fig. 4. Figure 9 shows that, in the dry lower-troposphere humidity scenario, the vertical velocity power spectrum at 9-km altitude is roughly characterized by a Kolmogorov $-5/3$ power law characteristic of isotropic turbulence at spatial scales smaller than approximately 200 m. A similar power law and scale break is seen in the variance spectrum for condensed water mixing ratio, suggesting that it is vertical dynamic motions (rather than latent heating) that governs condensate variability just above cloud base. There is a peak in variance associated with spatial scales between approximately 200 and 1000 m. These values lie within the range of 0.25–8 km normally attributed to mammatus (Schultz et al. 2006). Taking these values as indicative of a characteristic mammatus lobe diameter in the simulations, and assuming that the mixed layer circulations have an aspect ratio of approximately unity, then the diameter of the lobes should be related to their vertical displacement through a factor of approximately one-half. This would suggest that the depth of mammatus lobes should be approximately 1 km, a value that is roughly consistent with the mixed layer depth shown in Fig. 5 and the q_i cross-sectional plot shown in Fig. 8. The moist lower-troposphere scenario in Fig. 9 shows similar behavior to the dry scenario, except with a modest shift of dynamic variability to smaller spatial scales.

The above results suggest that, as described theoretically in section 2, $\Delta\tilde{T}$ between cloud base and the lower troposphere heats air near cloud base. The contrasts are greatest if the lower troposphere is dry and hence more thermally transparent. If the heating rates are sufficiently large and the cloud sufficiently wide [Eq. (8)], then air near cloud base becomes unstable and a deepening mixed layer develops. Mammatus-like lobes develop in this mixed layer, but not from a negatively buoyant instability below cloud base that is accelerated by evaporative cooling, as proposed previously by Emanuel (1981). Instead, they are part of this convecting mixed layer and are made more visible by entrainment of clear, dry air from below cloud base upward into the cloudy interior. The mixed layer depth and penetration distance of the ''cloud holes'' is highest in the dry scenario with the largest magnitude of $\Delta\tilde{T}$.

5. Visualization

Fundamentally, the definition of mammatus cloud is visual, not some prescribed variability in thermodynamic state. For assessment of the visual realism of numerical simulations of mammatus, a simple criterion is that model lobes of enhanced q_i must be sufficiently optically thick along their horizontal axis to be opaque to the lobes behind them.

Consider, for example, that optical depth is inversely related to cloud particle size:

$$\tau = \frac{3\rho q_i \Delta z}{2\rho_i r_e}, \tag{14}$$

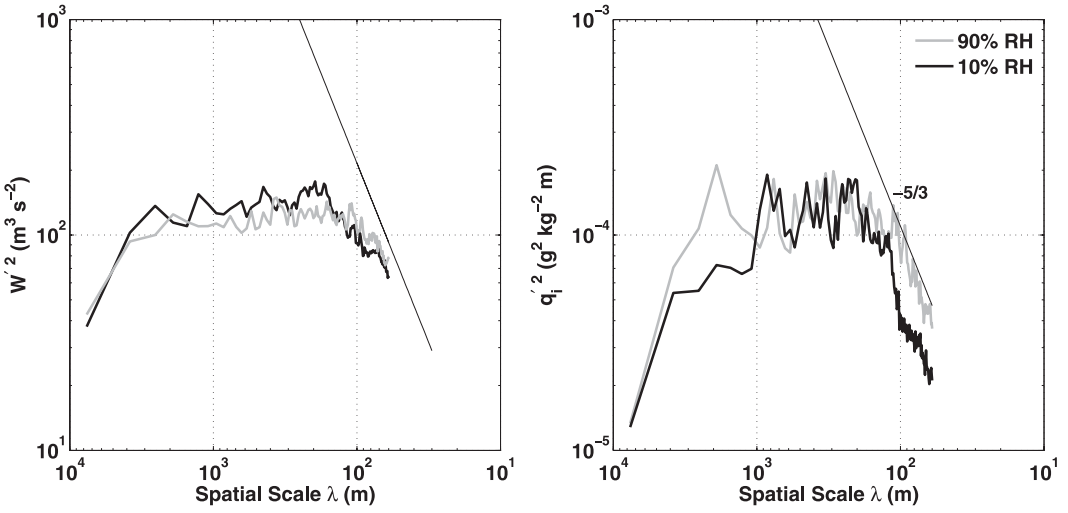

FIG. 9. Power spectra, as a function of spatial scale for (left) w and (right) q_i, for the moist (90% lower-troposphere RH) and dry (10% lower-troposphere RH) scenarios. Spectra are averaged for each of one hundred 30-m-wide annular transects between 4000- and 7000-m radius at 1-h model simulation time. The altitude of the spectra is 9000 m (just above cloud base).

where Δz is the lobe width, ρ_i the bulk ice density, and ρ the density of air. If, for example, one assumes values of q_i of ~0.5 g kg^{-1}, and a lobe diameter of 500 m, Eq. (14) requires for a mammatus lobe to be weakly ''opaque,'' say with $\tau = 3$, that r_e must be smaller than approximately 50 μm. Of course, very wide or dense lobes might contain larger crystals and still be opaque. However, it is probably safe to say that more modest mammatus lobes should contain ice crystals that are, on average, ''small'' and not be dominated by precipitation particles. Small crystal sizes satisfy several other criteria too: small crystals are a requirement for large heating gradients at cloud base [Eq. (4)] and they are more passive tracers of dynamic motions. Also, because the time it takes to evaporate cloud particles goes as the square of their size (Baker et al. 1980), small crystals sublimate more quickly, giving mammatus their ''smooth'' appearance (Emanuel 1981).

In the simulations shown here, the effective radius of ice crystals was fixed at 20 μm to be consistent with airborne measurements made in anvil cirrus (Garrett et al. 2005). To illustrate how the UU LESM simulations might appear visually, we passed the simulated q_i fields with r_e = 20 μm through a three-dimensional radiative transfer model [the Spherical Harmonics Discrete Ordinates Method (SHDOM); Evans 1998]. The light-scattering phase function used to simulate the radiative transfer is the inhomogeneous hexagonal monocrystal model (Labonnote et al. 2000). Several artificial ''tricks'' were necessary to make these simulations. These simulations are computationally intensive, so radiance fields were calculated for only one-quarter of the model domain. Also, mammatus clouds look most dramatic when an anvil base slopes slightly upward toward the direction of a setting sun, so that lobes are illuminated obliquely from below. Our simulations were initialized with a flat horizontal cloud base, and SHDOM does not permit illumination from below the horizon. Thus, to recreate mammatus illumination in SHDOM, what was necessary was to turn the cloud upside down and illuminate it from an oblique solar zenith angle of 80°. Here, also, the solar illumination azimuth is offset 60° from a direction directly behind the viewer.

The images for the two contrasting humidity cases are shown in Fig. 10. In the moist lower-troposphere scenario, mammatus lobes are only weakly apparent if at all. But they are quite clear in the dry scenario, even if they are not nearly as spectacular as is sometimes observed in nature.

One feature that is sometimes observed in mammatus cloud fields but was not reproduced here is ''streets'' or ''rows'' of mammatus lobes. Kanak and Straka (2009) showed that such organized structures can form in the presence of wind shear, provided it is not too much, in which case the mammatus lobes do not form at all.

6. Summary

A variety of possible explanations have been proposed for what leads to the formation of mammatus clouds (Schultz et al. 2006). The most widely accepted explanation is that they form through a cloud-base detrainment instability (CBDI) mechanism, as proposed by (Emanuel 1981) and simulated numerically by Kanak et al. (2008). Hydrometeors precipitate from cloud base and sublimate into subcloud air, which accelerates negatively buoyant thermals through evaporative cooling. If subcloud air is

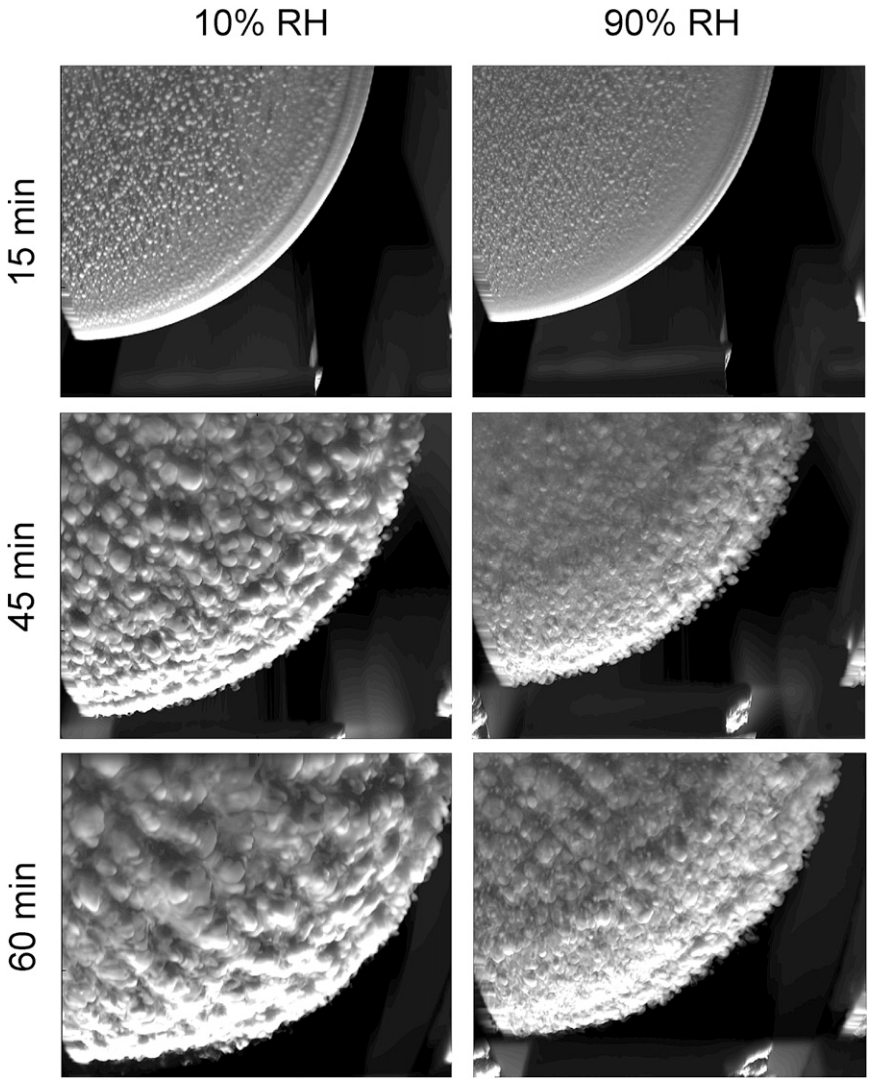

FIG. 10. Simulations using the SHDOM 3D radiative transfer model (Evans 1998) of the appearance of cloud base looking up for the cloud field shown in Fig. 3 for the (left) 10% and (right) 90% lower-troposphere humidity cases, calculated at three UU LESM time steps. Simulations are for one-quarter of the model domain. Bright spots in the lower-right-hand corner are due to this truncation.

dry, this aids sublimation and enhances the formation of the mammatus lobes.

In our study here, we attempted to simulate mammatus lobes in a cloud model with no sedimentation, production of precipitation turned off, and enhancement of sublimation immediately below cloud base minimized by high values of relatively humidity. The model was initialized with a cloud field that was horizontally homogeneous and neutrally buoyant. The cloud started to evolve only because thermal radiation emitted below the cloud was absorbed by cloudy air.

What was required for the cloud to develop mammatus lobes was large values of a ''spreading number'' $\mathcal{S}$ (Garrett et al. 2005), associated with clouds that are cold, wide, and thermally opaque, with visible optical depths greater than approximately 4. This combination leads to cloud-base heating that is sufficiently concentrated to overcome local gravitational stratification, causing clear air to be entrained from below cloud base. The clear air rises into the cloud interior in narrow ascending branches. Mammatus lobes are the visible, descending branches of this radiatively driven circulation, separated by the rising clear air. Over time, the turbulent layer and mammatus lobes deepen upward from the original cloud base. The mammatus lobes that were simulated have characteristics similar to those seen in observations, including being

associated with the presence of thin superadiabatic layers near cloud base. After being passed through a three-dimensional radiative transfer solver, the simulated lobes look like a fair representation of what is seen in nature.

We conclude from these idealized simulations that mammatus cloud can develop solely as a consequence of interactions between cloudy air and thermal radiation. In this regard, mammatus are perhaps an upside-down analog to the ''cloud holes'' seen descending from stratocumulus cloud tops. Like the rising clear-air branches separating mammatus lobes, stratocumulus holes do not appear to be driven by evaporative cooling (Krueger et al. 1995b), as in the cloud-top entrainment instability (CTEI) mechanism proposed by Randall (1980). Rather, they are driven by concentrated radiative cooling at cloud top (Gerber et al. 2005).

Our result does not exclude the possibility that some other mechanism like CBDI might trigger mammatus development (Schultz et al. 2006). In fact, it might be necessary to explain any observed situation where mammatus clouds descend well below the original anvil cloud base. However, we suggest that for any proposed mechanism to be viable, it should lead to cloudy lobes that are sufficiently optically dense to be opaque, as would be favored by the cloud particles being small. Ultimately, mammatus cloud is a visual classification.

That said, the simulations we show are of more ''garden-variety'' mammatus and are less developed than the extraordinarily deep and large lobes that are sometimes seen. However, we did identify a few ingredients that appear to be important for formation of large lobes. In our simulations, lobes were deepest when lower-troposphere air was driest, not because of enhanced sublimation but because the atmosphere was more radiatively transparent at thermal wavelengths; thermal contrasts between the cloud base and the below-cloud environment were enhanced, and these amplified the radiatively driven cloud-base instability. From theoretical arguments one would also expect mammatus to be favored by low static stability near anvil cloud base and high condensate mixing ratios. Also, since entrainment plays a role in helping to distinguish mammatus lobes, there may be an optimal level of relative humidity immediately below cloud base (Emanuel 1981). Below-cloud air should be dry to create distinctive lobes when it is entrained but not so dry that the cloudy lobes quickly sublimate through mixing.

Acknowledgments. The work was supported through Award NNX06AE24G through the NASA New Investigator Program. We wish to thank two anonymous reviewers and Jerry Straka for their reviews of the manuscript and appreciate discussions with Chris Garrett, Steve Krueger, and Dave Schultz.

REFERENCES

Ackerman, T. P., K.-N. Liou, F. P. J. Valero, and L. Pfister, 1988: Heating rates in tropical anvils. *J. Atmos. Sci.,* **45,** 1606–1623.

Arakawa, A., and W. H. Schubert, 1974: Interaction of a cumulus cloud ensemble with the large-scale environment, Part I. *J. Atmos. Sci.,* **31,** 674–701.

Baker, M. B., R. G. Corbin, and J. Latham, 1980: The influence of entrainment on the evolution of cloud droplet spectra: I. A model of inhomogeneous mixing. *Quart. J. Roy. Meteor. Soc.,* **106,** 581–598, doi:10.1256/smsqj.44913.

Cooper, S. J., and T. J. Garrett, 2010: Identification of small ice cloud particles using passive radiometric observations. *J. Appl. Meteor. Climatol.,* **49,** 2334–2347.

Dinh, T. P., D. R. Durran, and T. P. Ackerman, 2010: Maintenance of tropical tropopause layer cirrus. *J. Geophys. Res.,* **115,** D02104, doi:10.1029/2009JD012735.

Dobbie, S., and P. Jonas, 2001: Radiative influences on the structure and lifetime of cirrus clouds. *Quart. J. Roy. Meteor. Soc.,* **127,** 2663–2682, doi:10.1256/smsqj.57807.

Droegemeier, K. K., and R. B. Wilhelmson, 1987: Numerical simulation of thunderstorm outflow dynamics. Part I: Outflow sensitivity experiments and turbulence dynamics. *J. Atmos. Sci.,* **44,** 1180–1210.

Durant, A. J., W. I. Rose, A. M. Sarna-Wojcicki, S. Carey, and A. C. M. Volentik, 2009: Hydrometeor-enhanced tephra sedimentation: Constraints from the 18 May 1980 eruption of Mount St. Helens. *J. Geophys. Res.,* **114,** B03204, doi:10.1029/2008JB005756.

Emanuel, K. A., 1981: A similarity theory for unsaturated downdrafts within clouds. *J. Atmos. Sci.,* **38,** 1541–1557.

Evans, K. F., 1998: The spherical harmonics discrete ordinate method for three-dimensional atmospheric radiative transfer. *J. Atmos. Sci.,* **55,** 429–446.

Fu, Q., 1996: An accurate parameterization of the solar radiative properties of cirrus clouds for climate models. *J. Climate,* **9,** 2058–2082.

——, S. K. Krueger, and K.-N. Liou, 1995: Interactions of radiation and convection in simulated tropical cloud clusters. *J. Atmos. Sci.,* **52,** 1310–1328.

Garrett, T. J., 2008: Observational quantification of the optical properties of cirrus cloud. *Light Scattering Reviews,* Vol. 3, Praxis, 3–26.

——, and Coauthors, 2005: Evolution of a Florida cirrus anvil. *J. Atmos. Sci.,* **62,** 2352–2372.

——, M. Zulauf, and S. K. Krueger, 2006: Effects of cirrus near the tropopause on anvil cirrus dynamics. *Geophys. Res. Lett.,* **33,** L17804, doi:10.1029/2006GL027071.

——, M. M. Maestas, S. K. Krueger, and C. T. Schmidt, 2009: Acceleration by aerosol of a radiative-thermodynamic cloud feedback influencing arctic surface warming. *Geophys. Res. Lett.,* **36,** L19804, doi:10.1029/2009GL040195.

Gerber, H., G. Frick, S. P. Malinowski, J. Brenguier, and F. Burnet, 2005: Holes and entrainment in stratocumulus. *J. Atmos. Sci.,* **62,** 443–459.

Gu, Y., and K. N. Liou, 2000: Interactions of radiation, microphysics, and turbulence in the evolution of cirrus clouds. *J. Atmos. Sci.,* **57,** 2463–2479.

Hartmann, D. L., and K. Larson, 2002: An important constraint on tropical cloud–climate feedback. *Geophys. Res. Lett.,* **29,** 1951, doi:10.1029/2002GL015835.

Herman, G. F., 1980: Thermal radiation in Arctic stratus clouds. *Quart. J. Roy. Meteor. Soc.,* **106,** 771–780.

Heymsfield, A. J., 1986: Ice particle evolution in the anvil of a severe thunderstorm during CCOPE. *J. Atmos. Sci.,* **43,** 2463–2478.

——, and L. M. Miloshevich, 1991: On radiation and latent heat feedback in clouds: Implications and a parameterization. *J. Atmos. Sci.,* **48,** 493–495.

Kanak, K. M., and J. M. Straka, 2006: An idealized numerical simulation of mammatus-like clouds. *Atmos. Sci. Lett.,* **7,** 2–8, doi:10.1002/asl.121.

——, and ——, 2009: Effects of linear, ambient wind shear on simulated mammatus-like clouds. *Atmos. Sci. Lett.,* **10,** 226–232, doi:10.1002/asl.224.

——, ——, and D. M. Schultz, 2008: Numerical simulations of mammatus. *J. Atmos. Sci.,* **65,** 1606–1621.

Knollenberg, R. G., K. Kelly, and J. C. Wilson, 1993: Measurements of high number densities of ice crystals in the tops of tropical cumulonimbus. *J. Geophys. Res.,* **98,** 8639–8664.

Kollias, P., I. Jo, and B. A. Albrecht, 2005: High-resolution observations of mammatus in tropical anvils. *Mon. Wea. Rev.,* **133,** 2105–2112.

Krueger, S. K., Q. Fu, K.-N. Liou, and H.-N. S. Chin, 1995a: Improvements of an ice-phase microphysics parameterization for use in numerical simulations of tropical convection. *J. Appl. Meteor.,* **34,** 281–287.

——, G. T. McLean, and Q. Fu, 1995b: Numerical simulation of the stratus-to-cumulus transition in the subtropical marine boundary layer. Part II: Boundary-layer circulation. *J. Atmos. Sci.,* **52,** 2851–2868.

Labonnote, L. C., G. Brogniez, M. Doutriaux-Boucher, J.-C. Buriez, J.-F. Gayet, and H. Chepfer, 2000: Modeling of light scattering in cirrus clouds with inhomogeneous hexagonal monocrystals. Comparison with in-situ and ADEOS-POLDER measurements. *Geophys. Res. Lett.,* **27,** 113–116, doi:10.1029/1999GL010839.

Lilly, D. K., 1988: Cirrus outflow dynamics. *J. Atmos. Sci.,* **45,** 1594–1605.

Liou, K., 2002: *An Introduction to Atmospheric Radiation*. Academic Press, 583 pp.

Manabe, S., and R. F. Strickler, 1964: Thermal equilibrium of the atmosphere with a convective adjustment. *J. Atmos. Sci.,* **21,** 361–385.

Paluch, I. R., 1979: The entrainment mechanism in Colorado cumuli. *J. Atmos. Sci.,* **36,** 2467–2478.

Randall, D. A., 1980: Conditional instability of the first kind upside-down. *J. Atmos. Sci.,* **37,** 125–130.

Schultz, D. M., and Coauthors, 2006: The mysteries of mammatus clouds: Observations and formation mechanisms. *J. Atmos. Sci.,* **63,** 2409–2435.

Soden, B. J., 1998: Tracking upper tropospheric water vapor radiances: A satellite perspective. *J. Geophys. Res.,* **103,** 17 069–17 081, doi:10.1029/98JD01151.

Starr, D. O., and S. K. Cox, 1985: Cirrus clouds. Part II: Numerical experiments on the formation and maintenance of cirrus. *J. Atmos. Sci.,* **42,** 2682–2694.

Stephens, G. L., S.-C. Tsay, P. W. Stackhouse Jr., and P. J. Flatau, 1990: The relevance of the microphysical and radiative properties of cirrus clouds to climate and climatic feedback. *J. Atmos. Sci.,* **47,** 1742–1754.

Stith, J. L., 1995: In situ measurements and observations of cumulonimbus mamma. *Mon. Wea. Rev.,* **123,** 907–914.

Turner, J. S., 1979: *Buoyancy Effects in Fluids*. Cambridge University Press, 416 pp.

Winstead, N. S., J. Verlinde, S. T. Arthur, F. Jaskiewicz, M. Jensen, N. Miles, and D. Nicosia, 2001: High-resolution airborne radar observations of mammatus. *Mon. Wea. Rev.,* **129,** 159–166.

Yang, P., K. N. Liou, K. Wyser, and D. Mitchell, 2000: Parameterization of the scattering and absorption properties of individual ice crystals. *J. Geophys. Res.,* **105,** 4699–4718.

Zemanksy, M. W., and R. H. Dittman, 1997: *Heat and Thermodynamics*. 7th ed. McGraw-Hill, 487 pp.

Zulauf, M. A., 2001: Modeling the effects of boundary layer circulations generated by cumulus convection and leads on large-scale surface fluxes. Ph.D. thesis, University of Utah, 177 pp.